



HAL
open science

Time-resolved Dissolution Elucidates the Mechanism of Zeolite MFI Crystallization

Krassimir Bozhilov, Thuy Thanh Le, Zhengxing Qin, Tanguy Terlier, Ana Palčić, Jeffrey Rimer, Valentin Valtchev

► **To cite this version:**

Krassimir Bozhilov, Thuy Thanh Le, Zhengxing Qin, Tanguy Terlier, Ana Palčić, et al.. Time-resolved Dissolution Elucidates the Mechanism of Zeolite MFI Crystallization. *Science Advances*, 2021, 7 (25), 10.1126/sciadv.abg0454 . hal-03422955

HAL Id: hal-03422955

<https://hal.science/hal-03422955>

Submitted on 9 Nov 2021

HAL is a multi-disciplinary open access archive for the deposit and dissemination of scientific research documents, whether they are published or not. The documents may come from teaching and research institutions in France or abroad, or from public or private research centers.

L'archive ouverte pluridisciplinaire **HAL**, est destinée au dépôt et à la diffusion de documents scientifiques de niveau recherche, publiés ou non, émanant des établissements d'enseignement et de recherche français ou étrangers, des laboratoires publics ou privés.

Time-resolved Dissolution Elucidates the Mechanism of Zeolite MFI Crystallization

K. N. Bozhilov,^{1,†} T. T. Le,^{2,†} Z. Qin,³ T. Terlier,⁴ A. Palcic,⁵ J. D. Rimer,² V. Valtchev^{6,7*}

¹Central Facility for Advanced Microscopy and Microanalysis, University of California, Riverside, California 92521, USA

²University of Houston, Department of Chemical and Biomolecular Engineering, Houston, TX 77204, USA

³State Key Laboratory of Heavy Oil Processing, College of Chemical Engineering, China University of Petroleum (East China), Qingdao 266580, China

⁴Rice University, Shared Equipment Authority, SIMS laboratory, 6100 Main Street, Houston, TX 77005, USA

⁵Ruder Bošković Institute, Division of Materials Chemistry, Laboratory for Synthesis of New Materials, Bijenička cesta 54, Zagreb, Croatia

⁶Qingdao Institute of Bioenergy and Bioprocess Technology, Chinese Academy of Sciences, Qingdao, Shandong 266101, China

⁷Normandie Univ, ENSICAEN, UNICAEN, CNRS, Laboratoire Catalyse et Spectrochimie, 6 Boulevard Marechal Juin, 14050 Caen, France

* corresponding author's e-mail: valentin.valtchev@ensicaen.fr

† Authors contributed equally

Abstract

Zeolite crystal growth mechanisms are not fully elucidated owing to their complexity wherein the formation of a particular zeolite can occur by more than one crystallization pathway. Here we have conducted time-resolved dissolution experiments of MFI-type zeolite crystals in an ammonium fluoride medium where detailed structural analysis allowed us to extrapolate and elucidate the possible mechanism of nucleation and crystal growth. A combination of electron and scanning probe microscopy shows that dissolution initiates preferentially at lattice defects and progressively removes defect zones to reveal a mosaic structure of crystalline domains within each zeolite crystal. This mosaic architecture evolves during the growth process, reflecting the changing conditions of zeolite formation that can be retroactively assessed during zeolite crystal dissolution. Moreover, a more general implication of this study is the establishment that dissolution can be used successfully as an *ex situ* technique to uncover details about crystal growth features inaccessible by other methods.

Introduction

45 Zeolites are a family of crystalline microporous tectosilicates that are extensively used as
46 heterogeneous catalysts, molecular sieves, sorbents, and ion exchangers. The large-scale
47 production of synthetic zeolites already has more than a half-century history. At present,
48 the annual production is above 3 million tons per year (1). About ten different types of
49 zeolites are being used on a large industrial scale, and the number of zeolites used in niche
50 markets is larger. These figures demonstrate the maturity of large-scale production of
51 zeolites. Nevertheless, there are certain aspects of zeolite formation mechanism(s) that
52 remain to be clarified.

53 The difficulty in understanding zeolite crystallization is mainly due to the heterogeneity of
54 the growth mixtures containing solid and liquid components and the presence of a myriad
55 of different species (i.e., precursors) (2). The complex interactions between these species
56 and condensation steps leading to the formation of aluminosilicate frameworks around an
57 inorganic and/or organic structure-directing agent are also difficult to be traced and
58 unambiguously determined. Further uncertainty is compounded by the fact that the
59 formation of a particular zeolite could occur by more than one crystallization pathway (3-
60 5). Different methods providing information about the short- and long-range order in
61 aluminosilicates, their chemical composition, and molecular interactions have been
62 employed to shed light on the events preceding zeolite nucleation and the subsequent
63 growth process (2-11). Thus, zeolite formation has been studied by a variety of scientific
64 approaches to gain a more complete picture of the factors guiding the growth of a
65 particular zeolite. For instance, snapshots of a particular stage of zeolite formation were
66 obtained by *in situ* analysis using specially designed equipment (3, 4, 12). Molecular
67 modeling has also been used to decode zeolite formation in combination with
68 experimental analyses (13-15). These continuous efforts have resulted in a generally
69 accepted mechanism that describes the major stages of crystallization without, however,
70 being able to provide a basis for zeolite synthesis by design (10, 16).

71 Studies focused on characterizing local zeolite structure have allowed for identification of
72 the nucleation and growth of zeolites. Still, even these studies have not provided
73 molecular-level information on the various pathways involved in zeolite crystal growth (3,
74 4, 6, 7). Understanding the growth history and establishing a detailed picture of each stage
75 of zeolite formation would advance efforts to obtain a product with desired
76 physicochemical properties; however, such a thorough, comprehensive analysis of the
77 growth process for a single crystal is difficult to acquire with the currently available
78 methods.

79 In this study, we employ a non-traditional approach to study crystallization mechanisms:
80 dissolution in an ammonium fluoride medium. Dissolution offers a route to identify
81 defects or irregularities in crystals that form during growth where the chemical bonds that
82 break first would be corresponding to the weak bonds in the crystal. Following the critical
83 aspects of aluminosilicate dissolution, as summarized in detail by Crundwell (17-20), it is
84 considered that during dissolution experiments, the domains corresponding to stable,
85 viable nuclei should dissolve last. Hence, the dissolution of the zeolite structure can be
86 used to reveal information about the critical steps during nucleation and growth. Such an
87 approach allows for valuable insights of the growth process to be disclosed by identifying
88 regions with a high density of defects in the crystal and their role in various stages of
89 crystallization, i.e., the temporal trajectory of zeolite formation. The above presumption
90 could be correct only when the etching agent is not chemically selective and will not react
91 preferentially with the chemically inhomogeneous zones in the crystal (i.e. preferential

92 removal or Si or Al in aluminosilicates). This differs from the vast majority of processes
93 reported in literature where dissolution has been employed. For instance, etching is largely
94 used for the post-synthesis modification of zeolite properties (21-23). Steaming is a
95 commercial method for increasing the Si/Al ratio in zeolites (24, 25). Such a study
96 performed on a single zeolite particle level, using ZSM-5 as a model material, revealed
97 that the steaming renders its surface rough and generates mesoporosity (26). This greatly
98 improved the accessibility, but at the same time the strength of the Brønsted acid sites
99 decreased. Mineral acids are also used to extract Al from zeolite frameworks, while
100 caustic solutions are employed to preferentially remove Si (27-30); however, these
101 chemically selective etchants cannot be used to study the crystal growth of a zeolite.

102 Here we examine the unbiased dissolution of MFI-type zeolite crystals in a fluoride
103 medium at both macroscopic and molecular levels. Our recent results have shown that
104 upon dual hydrolysis, the compound NH_4F forms species that dissolve Si and Al at similar
105 rates (31). Etching by NH_4F was used to obtain hierarchical materials with retained
106 framework composition (32). In the present study, we have employed unbiased chemical
107 etching to reveal evidence of the zeolite crystallization mechanism. This process also
108 provides insights into the intimate structure of a crystal on the basis of molecular
109 reversibility since the weak bonds break first, and the stable, coherent domains dissolve
110 last, which allows for the facile detection of defects within the structure. This study is
111 performed on large crystals of ZSM-5 (Si/Al=91) and its siliceous isostructural form
112 silicalite-1, which allows for clearer visualization of any particularity in the growth
113 process. The use of a siliceous and Al-containing sample was necessary to evaluate the
114 impact of aluminum on the growth and respectively on the dissolution process. For the
115 sake of comparison, a low silica ZSM-5 material (Si/Al=21) synthesized in a basic
116 medium was also included in the study.

Results

From powder XRD analysis, the sharp peaks in XRD spectra showed that all employed MFI samples are highly crystalline (Fig. S1A). The N₂ adsorption-desorption isotherm (Fig. S1B) is type I, which is characteristic of microporous materials. The micropore volume of MFI-type materials, calculated using the t-plot method, is ca. 0.16 cm³/g, a value typical for highly crystalline MFI-type materials. SEM inspection revealed that the ZSM-5(91) crystals are uniform in size and approximately 100-120 μm in length (i.e., the c-direction, Fig. S1C). Silicalite-1 crystals synthesized in fluorine medium are a little bit shorter, ranging between 80 and 100 μm. ZSM-5(21) sample also exhibits well-shaped crystals with a size of about 5 μm. The majority of crystals have well-defined morphology with the typical coffin shape, and a few agglomerates can be observed.

The surface features of ZSM-5(91) crystals from SEM are shown in Fig. 1A. Different levels of crystal etching, from the as-synthesized sample until later times when the initial crystal morphology is indiscernible, are presented in Fig. 1C-F. After 30 min treatment in NH₄F, only the interface between twinned zeolite crystals is dissolved, as can be seen in Fig. 1B, showing the dissolved interface between two contact twins oriented at 180° relative to each other. Fig. 1C shows the dissolution of the interface between an 80 μm long crystal and surface twins rotated at 90°. After 60 min treatment, deeper dissolution reveals interior features building the apparent “single” crystals (Fig. 1D); and after 120 min etching, only fragments of the original crystal remain where cavities with angular outlines can be seen (Fig. 1E, F). These observations show that the dissolution process is steered by distinct crystallographic zones with a clear hierarchical organization. Namely, at the micron scale, the interfaces between the twin crystals are preferentially dissolved (Fig. 1B-D), and on a nanometer scale, the dissolution follows particular crystallographic directions since dissolution pits exhibit well-defined straight facets, with pseudo-hexagonal shape (Fig. 1 and 3). Furthermore, we observe that the crystal core is more extensively dissolved than the peripheral regions of the crystals. In order to better understand the phenomenon controlling the dissolution process, complementary imaging methods were employed.

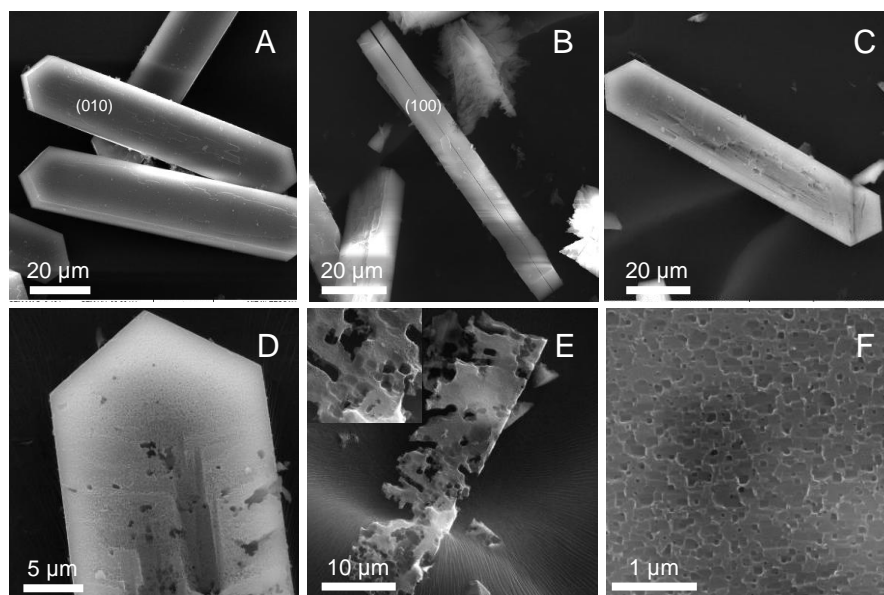
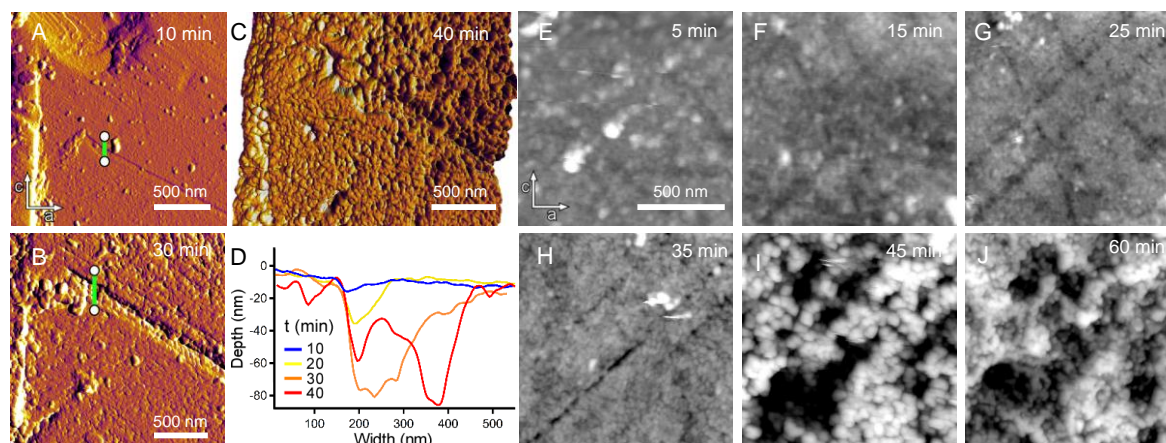


Fig. 1. Scanning electron micrographs of parent ZSM-5(91) and partially-dissolved crystals obtained after different periods of etching. (A) Parent crystals used for the dissolution experiments; (B) morphology and features of reaction products after 30 min dissolution; (C) representative crystal subjected to 60 min treatment; (D) higher magnification view of the (010) facet of a crystal after 60 min treatment; (E) representative crystal subjected to 120 min treatment; and (F) high magnification view of the (010) surface of a crystal after 120 min etching.

Atomic force microscopy (AFM) was used to examine time-resolved changes in surface topography during crystal dissolution. Conducting *in situ* measurements was challenging due to the debris generated at the interface; therefore, we employed an *ex situ* protocol (Scheme S1) wherein the same surface of a zeolite crystal was imaged after various intervals of NH_4F treatment (Fig. S2). After each interval of the treatment, a series of AFM images were taken over an entire (010) surface and combined into a composite figure (Figs. S2 and S3A), where specific regions could be evaluated to track distinct changes in surface features with time. There were three general types of features observed in AFM images: crevices, etch pits, and spheroidal domains. The generation of crevices (Fig. 2A – C) seem to originate at (100) edges of the crystal and propagate inward with temporal increases in crevice width and depth (Fig. 2D). Multiple *ex situ* images of the crystal surface were compiled in Movie S1 where periodic snapshots during 60 min of treatment (Fig. 2E – J) reveal significant changes in surface topography. The initially rough surface of the untreated crystal becomes relatively smooth after 10 min of treatment due to the removal of large features present on as-synthesized substrates; and with prolonged treatment, AFM images reveal the emergence of crevices and etch pits. Similar to FE-SEM images in Fig. 1, we observe heterogeneous surface topographies with prolonged dissolution time. Some regions remain relatively smooth with less evidence of dissolution, whereas other regions develop highly roughened or pitted surfaces (Fig. S2). Images after 45 min of treatment (Fig. 2I) show the presence of spheroidal domains and etch pits that become enlarged with further treatment (Fig. 2J). The size distribution of etch pits after 60 min of NH_4F treatment is shown in Fig. S2. The AFM analysis demonstrates the inequivalent spatial dissolution of the zeolite crystal surface, which is not

180 related with the framework composition since this series of experiments was performed on
181 silicalite-1 crystals. Thus, surfaces exhibiting disproportionately high rates of dissolution
182 is attributed to zeolite crystal imperfections (i.e., defect zones present on crystal facets).



184
185 **Fig. 2. AFM analysis of silicalite-1 (010) surface dissolution for the area marked in**
186 **Fig. S3A.** (A and B) Time-elapsing images between 10 to 30 min of treatment showing the
187 development of a crevice. (C) 3-dimensional rendering of overlapping height and
188 amplitude images showing the crevice after 40 min of treatment. (D) Height profiles along
189 the green lines in A and B showing the increased depth and width of the crevice with
190 treatment time (data are normalized to the baseline). (E – J) Height images of a different
191 surface between 5 to 60 min of treatment at a fixed imaging area (highlighted in Fig.
192 S3A). The full sequence of time-resolved images is compiled in Movie S1.

193
194 Later stages of dissolution, when etch pits became too deep for analysis by AFM, were
195 studied using a combination of SEM, TEM, and STEM. Representative images of ZSM-
196 5(91) and silicalite-1 crystal dissolution after 30 and 60 min are shown in Fig. 3A-C and
197 Fig. 3D-F, respectively. The backscattered-electron (BSE) image of ZSM-5(91) (Fig. 3A)
198 and TEM bright-field image of silicalite-1 (Fig. 3D) both reveal zonal growth patterns. In
199 particular, the hour-glass feature (Fig. 3D) suggests sectorial growth starting from the
200 crystal core, consistent with previous studies of large MFI-type crystals (33). Electron
201 micrographs showed that the dissolution along the interface between the 90° and contact
202 twins in ZSM-5(91) crystals is due to the presence of highly strained zones between the
203 individual crystals; however, the origin of small etch pits with pseudo-hexagonal shape
204 formed deep within the core of the crystals is not immediately obvious. It is revealed (Fig.
205 3C and F) that the facets outlining the etch pits are parallel to low index atomic planes,
206 such as (001) and (101); clearly exhibiting crystallographic control of dissolution on the
207 unit cell level.

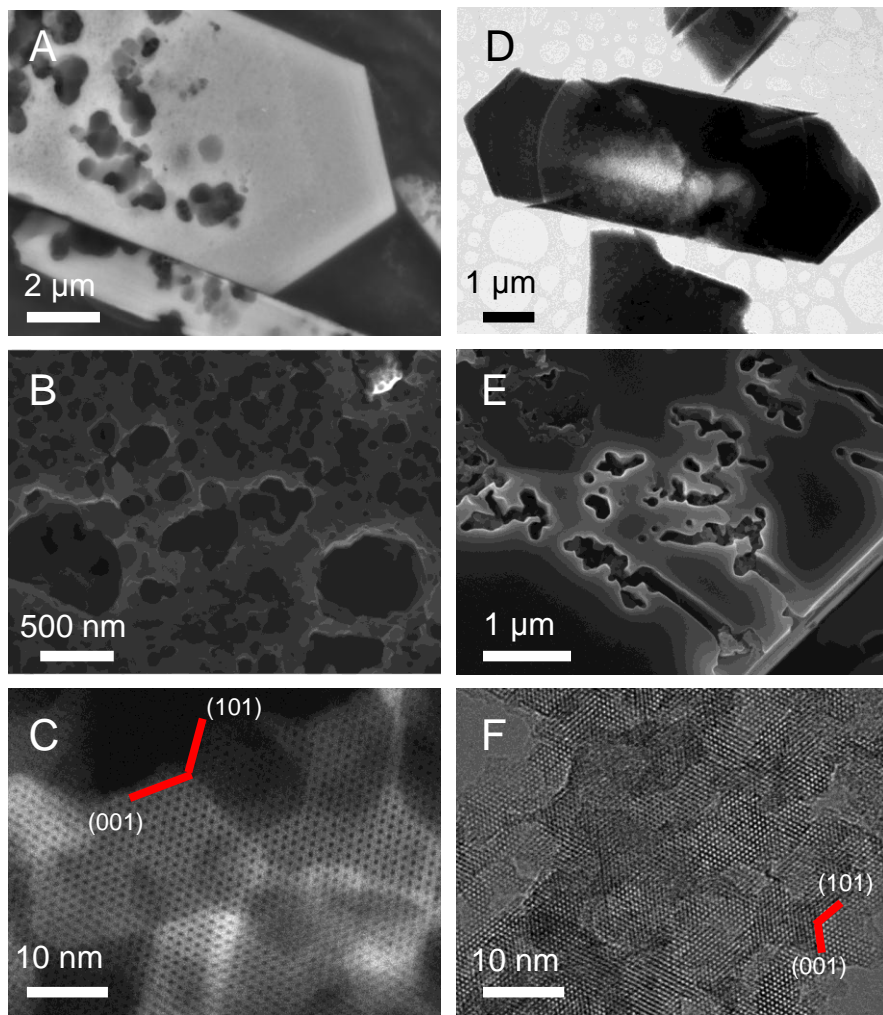


Fig. 3. Dissolution uncovers the history of ZSM-5(91) and silicalite-1 crystallization.

(A) Zonal growth structure in the later growth stages is revealed by BSE imaging of ZSM-5(91) crystal treated for 30 min. (B) SEM image of ZSM-5(91) crystal treated for 60 min highlighting dissolution pits on the {010} face with pseudo-hexagonal shapes and straight edges parallel to low index atomic planes, such as {001}, {101}, and $\{10\bar{1}\}$. (C) HAADF HR-STEM image along the $\langle 010 \rangle$ axis of the same specimen shown in (B). The dark spots in the structural images correspond to the channels in the structure, and the bright lines are the SiO₄ tetrahedral chains. (D) TEM bright-field image of a silicalite-1 crystal treated for 60 min. (E) SEM image of the {010} face of a silicalite-1 crystal treated for 30 min revealing the pseudo-hexagonal shape of dissolution pits that appear more irregular than those of ZSM-5(91). (F) Corresponding HR-TEM image down the $\langle 010 \rangle$ axis from the same specimen in (E). The bright spots here correspond to the open channels of the zeolite structure and the dark areas to the framework. The orientation of the traces of the {001} and {101} planes are marked with red lines in (C) and (F).

In a previous study, we suggested that the mosaic of pseudo-hexagonal etch pits might be due to the dissolution of misoriented crystalline domains. Here, this hypothesis is verified by HRTEM imaging down the c-axis of ZSM-5(91) crystal. As shown in Fig. 4, thin electron transparent lamellas were cut perpendicular to the c-axis by focused ion milling from two different regions of the same crystal. The first lamella was cut from the peripheral region of the crystal close to the apical tip (Fig. 4A, C, and D), labeled as “I” in the inset of Fig. 4. The second was cut from the central part of the crystal (Fig. 4B, E, and

F) and is labeled “IP”. The crystal structure and order in lamella I appears perfect with no significant defects or distortions (Fig. 4A), also confirmed by the sharp, bright spots in the corresponding fast Fourier transform (FFT) pattern (Fig. 4C). In contrast, closer inspection of HRTEM images of lamella II (Fig. 4B) reveals the existence of a mosaic structure in the center of the crystal that is comprised of fine domains slightly misoriented with respect to each other by minor mutual rotation within the plane of imaging. The fine domains are confirmed by both dark-field contrast imaging (Fig. 4E) utilizing (020) reflections as well by the shape and size of the (010), (020) and (200) reflections in the FFT pattern (Fig. 4F). The diffuse character of the spots in Fig. 4F can be attributed to misorientation between the fine domains in this region of the crystal. A comparison between the same type of reflections (marked by white arrows in Fig. 4C and 4F, respectively) demonstrates the difference in crystalline ordering of the peripheral and central parts of the crystal. The sharp character of the FFT spots in Fig. 4C is clear evidence of a defect-free structure as opposed to the mosaic domain structure revealed in Fig. 4F.

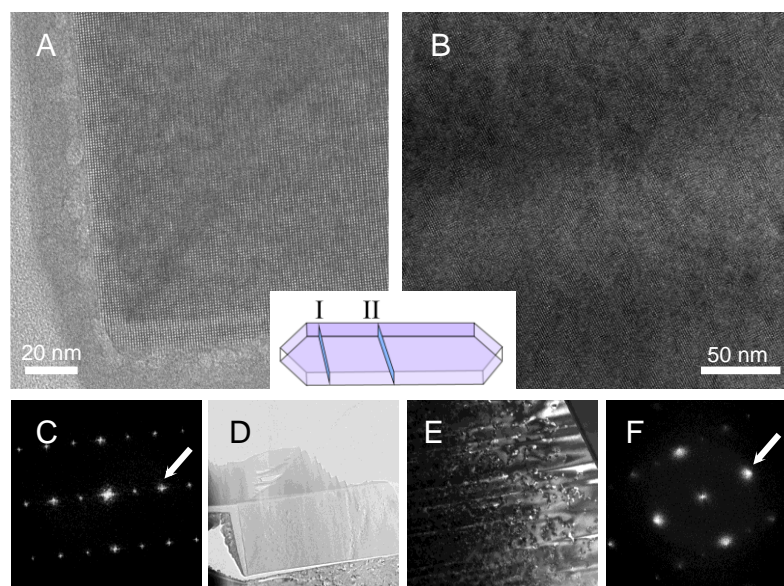


Fig. 4. TEM images of FIB thin sections cut perpendicular to the c-axis from an as-synthesized ZSM-5(91) crystal not subjected to dissolution treatment. HRTEM images down the c-axis of foils from the periphery (A) and the central part (B) of the crystal. (C and F) FFTs from the lattice images in (A) and (B), respectively, with marked (020) reflections. (D) Low magnification image of one of the FIB foils. (E) Low magnification TEM dark-field image from the foil cut from the central part of the crystal. Inset: schematic of the sites for cutting sections I (periphery) and II (center) from the as-synthesized crystal.

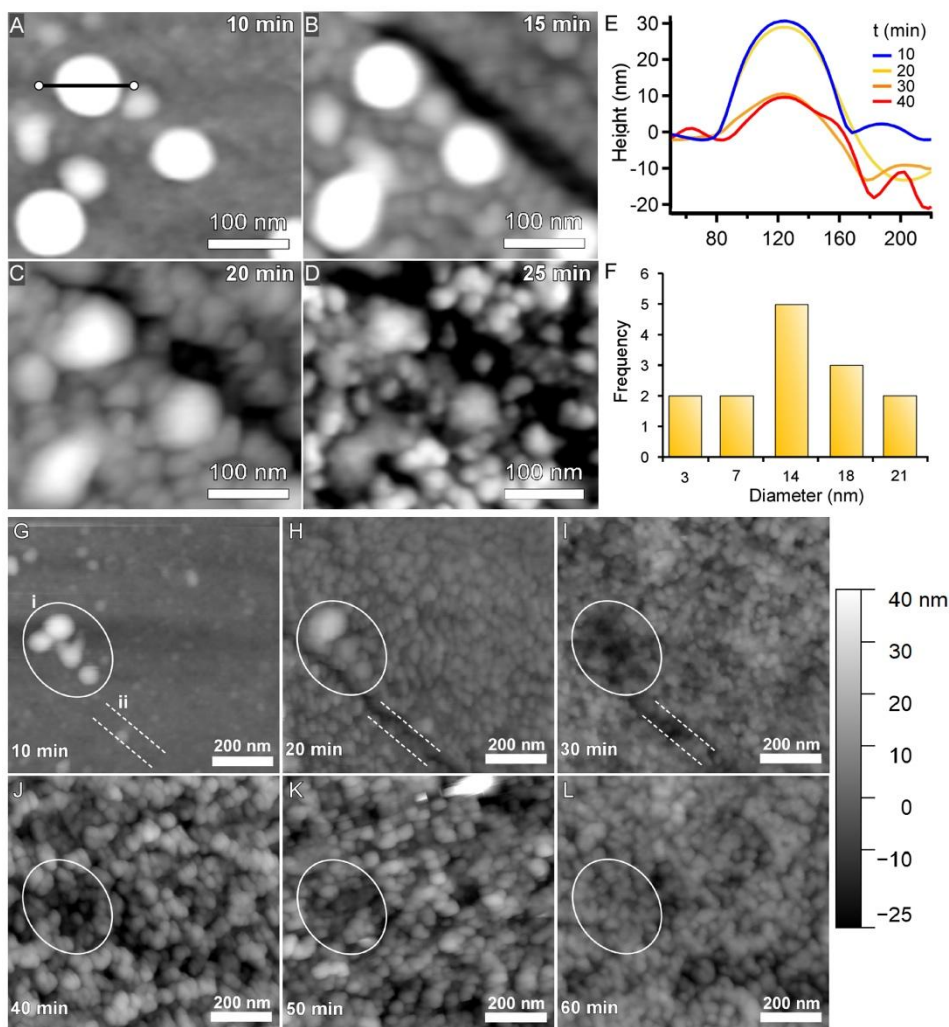
The above interpretation is further corroborated by cutting a thin FIB section perpendicular to the c-axis from the middle of another ZSM-5(91) crystal (Fig. S4). The misorientation between adjacent domains is minor and difficult to discern directly from HRTEM images. As such, the same digital processing was applied to the images taken in the middle and the periphery of the foil (cut from the central part of untreated ZSM-5 crystal) to enhance the contrast. First, FFT was applied to the HRTEM images to obtain

262 the patterns shown in Fig. S4C and D, then a circular filter was applied to select only the
263 reflections up to (200) and (020) in the FFT patterns (insets in Fig. S4C and D). Inverse
264 FFT processing of the aforementioned filters resulted in the images shown in Fig. S4A and
265 B. The uniform appearance of the filtered inverse-FFT image in Fig. S4B (i.e. the lack of
266 contrast variation across the lattice fringes), in comparison to the nonuniformity of the
267 image of the central part (Fig. S4A), confirms the defect-free nature of the peripheral parts
268 of the ZSM-5(91) crystals. This is consistent with the sharp reflections seen in the FFT
269 pattern from the periphery (Fig. S4D) compared to the more diffused appearance of the
270 FFT reflections (Fig. S4C) from the HRTEM image of the central region. Fine domains
271 between 10 and 25 nm in diameter are visualized by HRTEM imaging after processing in
272 the central part of the thin foil (Fig. S4A and C), revealing the mosaic structure of the
273 central region of ZSM-5(91) zeolite crystals due to minor misorientation of neighboring
274 domains. Such domains are missing in the periphery of the foil (Fig. S4B and D),
275 indicating this region possesses little to no defects.

276 The difference in the dissolution of the peripheral and central parts of the crystal is also
277 observed by chemical mapping via time-of-flight secondary ion mass spectrometry (ToF-
278 SIMS) of untreated silicalite-1 crystals (Fig. S5A-D) compared to those after 60 min of
279 treatment (Fig. S5E-H). The trace quantity of the organic structure-directing agent
280 (tetrapropylammonium, TPA) provides a high contrast wherein the tracking of TPA ion
281 fragments ($C_3H_8N^+$) in the crystal before and after treatment (Fig. S5B and Fig. S5F,
282 respectively) reveals distinct regions of dissolution. Similar information with less
283 sensitivity can be gleaned from ToF-SIMS mapping of SiO^+ (Fig. S5 C and G) and
284 Si_2OH^+ (Fig. SD and H) ions, which reveal a difference in Si-O bonds and terminal silanol
285 groups between the peripheral and central regions of the silicalite-1 crystals. In addition,
286 we used *ex situ* AFM to monitor the evolution of spheroidal domains during NH_4F
287 treatment of a silicalite-1 (010) surface. High-resolution images of a fixed area on the
288 crystal surface (Fig. 5A-D and Movie S3) reveals the progressive appearance of small
289 spheroidal domains that seemingly dissolve at a much slower rate than the surrounding
290 regions (Fig. 5G). Similar features were observed in multiple regions of several crystals
291 during AFM measurements (e.g., Fig. 2I and Movie S1). Analysis of height images for
292 several crystals in a single dissolution experiment reveals a distribution of spheroidal
293 feature sizes (Fig. 5F) with an average diameter of 15 nm. This is consistent with the
294 domain sizes determined by HRTEM imaging (Fig. S4) corresponding to interior regions
295 of the crystal, where more defects are observed. The classification of spherical domains as
296 either amorphous or crystalline cannot be gleaned from AFM images; however, we
297 surmise these features are predominantly crystalline on the basis of several observations.
298 First, the size of spheroidal features is much larger than those of amorphous precursors
299 typically encountered in MFI synthesis, which range from 1 to 6 nm (34). Previous in situ
300 AFM measurements (3) have shown that the attachment of amorphous precursors to MFI
301 crystal surfaces is followed by a disorder-to-order transition wherein precursors become
302 integrated into the underlying crystal interface. It is possible that a fraction of amorphous-
303 to-crystalline transformations are incomplete, leading to the occlusion of disordered
304 domains as defects within zeolite crystals. We posit these events are rare, and do not
305 account for the large population of 15 nm spheroidal domains observed in AFM images
306 (Figs. 2 and 5). This is consistent with HRTEM images (Figs. 3 and 4) that lack evidence
307 of amorphous domains, which would be expected to extend well beyond that of a single
308 particle to encompass the large areas observed in AFM images (e.g. Fig. 5J) with high
309 densities of spheroidal features. As such, these spheroidal features are likely crystalline

310
311

nanoparticles that incorporate into zeolite crystals via a mechanism of (nearly)oriented attachment.



312

313

314

315

316

317

318

319

320

321

322

323

324

325

326

327

328

329

330

Fig. 5. AFM analysis of the dissolution of silicalite-1. (A – D) AFM height images of a fixed area on a silicalite-1 (010) surface between 10 and 25 min of treatment. The images were taken from the region highlighted in Fig. S3A, and the full compilation of time-resolved images is compiled in Movie S2. (E) Height profiles of a feature in AFM images (marked with a black line) after the following treatment times: 10 min (blue), 15 min (yellow), 20 min (orange), and 25 min (red). (F) Analysis of AFM images over the entire crystal surface after 60 min of treatment reveals a distribution of spheroidal feature diameters ($n = 17$ measurements). The diameters are median values (± 2 nm) adjusted to account for the AFM tip curvature (see Scheme S1B). (G – L) AFM height images of a fixed silicalite-1 (010) surface area between 10 and 60 min of treatment. A full compilation of time-resolved images (5 min intervals) is shown in Movie S3. The color gradient, which correlates to height (nm) is constant for all images. Several features (white oval, *i*) during dissolution alternate between smooth to rough topographies as spheroidal features progressively emerge from the dissolving interface. These images also show a crevice (double white dashed lines, *ii*) that becomes less prominent with prolonged treatment as the difference in height between the depth of the crevice and the crystal surface decreases. A corresponding set of amplitude images is included in Fig. S6. The area selected for analysis is marked in Fig. S3A.

332 The crystal growth pattern of MFI-type zeolite is clearly revealed by dissolution
333 experiments. As shown in Figs. 3 and S5, the interior regions of the crystal dissolve much
334 more rapidly than the periphery. Furthermore, TEM imaging clearly reveals an “hour-
335 glass” feature in the center of the majority of partially-dissolved crystals. This hour-glass
336 zone is overgrown by zonal features (Fig. 3A and D). The above observations are
337 evidence of multi-stage crystal growth, where the growth mechanism changes from
338 sectorial to zonal growth over the course of crystallization.

339 The characteristics of late-stage zonal growth are further exhibited by a closer
340 examination of temporal changes in surface topography of facets during the final growth
341 stages. The growth terraces visualized in SEM images (Fig. S7) demonstrates, first, that
342 the growth at this stage proceeds by the layer-by-layer zonal growth mechanism. Second,
343 it shows that the growth most probably takes place by agglomeration of viable globular
344 proto-crystals with sizes between 5 to 25 nm in diameter, rather than direct incorporation
345 of dissolved ionic or molecular species from the solution.

346 AFM imaging (Fig. S2) also confirms the presence of non-uniform regions (micron-size
347 areas) where dissolution is more prevalent in some locations, whereas others are less
348 affected by the treatment. Time-resolved analysis of the silicalite-1 (010) surface during
349 dissolution also reveals dynamic sequences of emerging and disappearing features leading
350 to either smooth or rough surface topography. For example, AFM height images of a fixed
351 area over a 60-min period of dissolution (Figs. 5G-L) and corresponding amplitude images
352 (Fig. S6) reveal the initial presence of large protrusions (highlighted by the dashed oval)
353 that disappear with treatment time to yield an interface with either flat regions or
354 spheroidal features.

355 Discussion

357 The applied approach has allowed us to reveal critical details about the zeolite dissolution
358 process and, in turn, about the intimate structure of the studied MFI-type materials. The
359 following conclusions can be drawn regarding the dissolution process. Dissolution is
360 selective for regions with higher densities of defects, which are non-uniformly distributed
361 throughout the crystal. The etching agent attacks predominantly the central parts of the
362 MFI-crystals and affects the periphery of crystals to a significantly lesser extent, which
363 corresponds to their relative concentration of defects (Figs. 4 and S4).

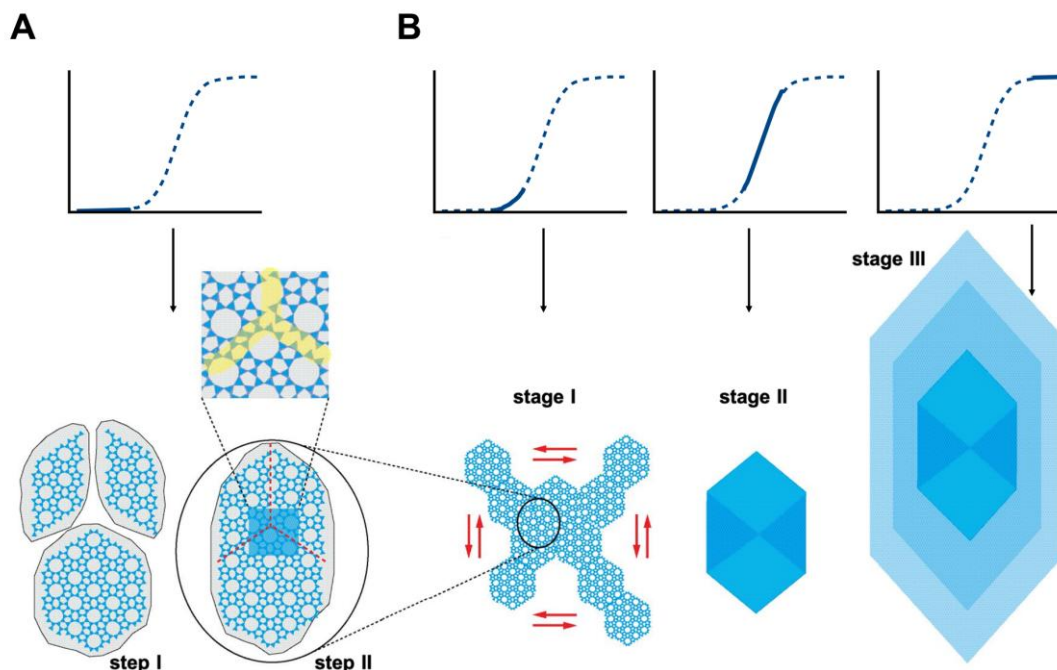
364 Our analyses have shown that the crystals are chemically homogeneous and structurally,
365 on a micron-scale level, are well crystallized with some degree of twinning. The studied
366 MFI-type samples are essentially built up by SiO_4 tetrahedra, where all oxygen atoms are
367 shared. Hence, there is no significant structural anisotropy in the bond strength across
368 individual tetrahedra, which can affect the dissolution process (17-20). The main factor
369 that would affect Si-O bond strength is protonation; however, since the crystal is
370 compositionally homogeneous, protonation should not affect the dissolution process
371 selectively. Consequently, the primary cause of dissolution is the presence of defects on
372 atomic and unit cell levels, which can introduce inhomogeneity and selective bonding
373 among the SiO_4 tetrahedral framework. Different types of defects in crystalline materials
374 are presented in Scheme 2. Our observations suggest that dissolution starts at defect sites
375 with strained T-O bonding, such as point defects, dislocations, twin boundaries, and low-

376 angle grain boundaries. It proceeds by expanding around initially formed dissolution pits.
377 The dissolution advances parallel to low-index atomic planes with small reticular density,
378 which seemingly follows a reciprocal Bravais-Friedel-Donnay-Harker (BFDH) growth
379 law (35) at a localized level. The BFDH growth law stipulates that the morphological
380 importance of crystal faces is reciprocally proportional to the reticular density of the
381 atomic planes, expanded later by Hartman and Perdok (36), relating the reticular density to
382 the crystal bond strength between building constituents. The crystal periphery appears to
383 be the most stable, which accounts for our observation that this region dissolves at a much
384 slower rate. In the late stages of zeolite formation, the growth rate is relatively slow and
385 likely accounts for the presence of fewer defects in peripheral crystal zones, thereby
386 leading to higher structural order in these regions (Figs. 3, 4, and 5).

387 Our previous study of zeolite LTA showed that nucleation occurs within agglomerates of
388 amorphous (alumino)silicate precursors (6). The latter species coalesce with synthesis
389 time into larger particles with a crystalline structure and an overall size of a few to tens of
390 nanometers, forming stable nuclei that can interact and fuse with other nuclei throughout
391 the crystallization process. A similar process for MFI-type zeolite was reported (37) using
392 cryo-TEM to track various stages of nucleation to confirm growth by a nonclassical multi-
393 step mechanism (38). Following the above observations as well as those from this study,
394 our interpretation of the nucleation and crystallization process is summarized
395 schematically in Fig. 6. The initial incubation period is marked by the formation of fine
396 crystalline proto-particles (Fig. 6A, step I). During the coalescence of these particles, the
397 formation of domain boundaries (marked by red dashed lines in Fig. 6A, step II) is
398 proposed where the fast fusion between them creates a mismatch between the crystalline
399 structure of each particle. The process is statistical in nature; some of the discrepancies
400 and distortions that have higher interface energy are eliminated by minor re-arrangements;
401 others are sealed and preserved as fine-size domains through the subsequent stages of
402 crystal growth. Some of these intergrowing domains give rise to twin relationships and
403 likely serves as a starting point for twin growth; others have mismatch that leads to low-
404 angle domain boundaries, dislocations, and point defects. The vacancies between
405 crystalline domains can be sealed by the addition of low molecular weight
406 (alumino)silicates (i.e. monomers or oligomers) through crystallization by particle
407 attachment involving the addition of amorphous precursors. The central region of the
408 zeolite crystal forms fast due to a high initial supersaturation (including amorphous
409 precursors and soluble species) and a large number of crystallites present, which tends to
410 concentrate a high level of defects, which is an anticipated for crystallization by particle
411 attachment (38). Moreover, nonclassical pathways involving the addition of amorphous
412 precursors can also lead to defects if the disorder-to-order transition is either incomplete or
413 results in misoriented crystalline domains.

414 Many of the observations from the study of MFI dissolution are consistent with the
415 processes of zeolite crystallization outlined above. Preferential dissolution at the center of
416 the crystal agrees with the higher number of defective zones created during the early
417 stages of zeolite formation via the agglomeration of MFI nanocrystallites. Consequently,
418 the central part of the crystal is more vulnerable to etching and dissolves more rapidly. It
419 is apparent that zeolite formation in the studied system is a complex multistage process, as
420 the mechanism of growth is a function of the supersaturation, which differs in the early
421 and late stages. It can be speculated that the initially formed nuclei rapidly assemble into a
422 skeletal structure along the $\langle 101 \rangle$ directions (stage 1 in Fig. 6B), setting up the growth
423 process of the subsequent stage 2 that proceeds by sectorial growth originating from the
424 skeletal structures formed in stage 1 (stage 2 in Fig. 6B and 3D). This is facilitated further
425 by the high concentration of nuclei present in the solution. The final stage is marked by a

426 lower concentration of reactive species and a slower growth rate, leading to peripheral
 427 regions with fewer defects that exhibit slower rates of dissolution. The large size of the
 428 crystallites formed already predetermines zonal layer-by-layer growth (39) following rapid
 429 nucleation and growth in the crystal core. The participation of the pre-formed particles,
 430 which we evaluated to be in the range of 5 to 25 nm (Fig. 3C and F, 5F, S4A), is limited
 431 during the late stage of zeolite growth. growth and dissolution are competing processes
 432 resulting in the final crystal form, which is faceted by low index slow-growing faces.
 433



434
 435 **Fig. 6. Schematic drawing of the interpretation of the growth process in the studied**
 436 **MFI-system.** (A) The incubation process involves two steps: (I) formation of proto-
 437 particles with MFI structure; (II) fusion of these particles to form nuclei. Structural
 438 discrepancy boundaries are marked with broken red lines. The shaded central part of the
 439 nucleus corresponds to the enlarged inset, and the structural discrepancy boundaries are
 440 marked in yellow. (B) The growth process has three distinct stages: (I) skeletal growth,
 441 (II) sectorial growth, and (III) final zonal overgrowth. Each phase is correlated with the
 442 crystal growth period in the crystallization curve depicted in the top part of the scheme.
 443

444 The reported results were obtained by studying large zeolite crystals grown in a fluoride
 445 medium. The validity of the findings was verified by a study on conventional ZSM-5(21)
 446 crystals synthesized in a basic medium. The small crystals size (ca. 5 μm) is not
 447 appropriate for an AFM investigation. Thus the dissolution process was followed by a
 448 combined SEM-TEM analysis. Representative SEM and TEM micrographs of the crystals
 449 subjected to 20, 40, and 60 min 40 wt. % NH_4F solution etching are shown in Figure S8.
 450 After 20 min etching, the twin crystals were separated (Figure S8B). Also, the extremity
 451 of the crystals, which are formed during the slower zeolite growth in the later stages, were
 452 often separated from the core (Figure S8 D). After 40 min etching, the central part of the
 453 crystals, which forms during the period of high supersaturation and abundant nucleation
 454 (see Figure 6A) and thus containing a higher number of defective zones, was deeply
 455 etched Figure S8 C,E. It should be noted the exceptional etching resistance of the surface
 456 layer (Figure S8 C,E) formed during the zonal growth (see Figure 6, stage III). However,

457 the thickness of this layer, which is a result of the zonal overgrowth, was only about 50
458 nm, while in the case of fluoride medium-grown crystals, it was several microns (Figure
459 3A). Deeply etched ZSM-5(21) crystals exhibit a mosaic of rectangular dissolved domains
460 (Figure S8E). Similar dissolution profiles were observed in the large fluoride medium
461 synthesized ZSM-5 crystals Figure 1F. Thus the comprehensive electron microscopy study
462 revealed that the conventional ZSM-5(21) grown in basic medium exhibit the same
463 dissolution profile as the high silica ZSM-5(91) and all-silica (silicalite-1) counterparts
464 synthesized in fluoride medium. This is unambiguous proof of the general dissolution
465 mechanism, which allows recovering the zeolite's growing history, reported in the present
466 study.

467 **Conclusion**

469 This study has shown that studying dissolution reactions can be used successfully as a
470 powerful tool to reveal the processes of nucleation and crystal growth down to the atomic
471 level, which are difficult processes to assess in hydrothermal systems by the presently
472 available *in situ* methods. Furthermore, the vast majority of available *in situ* methods are,
473 in principle, either of bulk nature or only capable of providing resolution at micron or
474 larger scale, which prevents direct assessment of the growth process.

475 The dissolution of MFI-type crystals revealed defects of different types; however, the
476 dominant form of defects and its corresponding concentration and spatial distribution are
477 highly dependent upon the “history” of the growing crystals. The stochastic nature of
478 zeolite nucleation and crystal growth leads to particles containing disparate populations of
479 structural defects. The initial period of rapid nucleation in highly supersaturated media
480 generally increases the probability of high defect density within the interior of zeolite
481 crystals, whereas slower growth rates occurring by classical crystallization at later stages
482 of synthesis (i.e., when the nutrient pool is depleted) leads to fewer defects. Thus, the
483 memory of the growth process is coded in the crystal, and the method employed in this
484 study using dissolution enables the recovery of a zeolite's growth history.

485 In addition, more general implication of our observations concerns the mosaic structure in
486 crystals that has been known for a long time (40), but no direct correlation of its effect on
487 the growth mechanism of microcrystals has been demonstrated until now.

489 **Materials and Methods**

491 *Zeolite synthesis*

492 ZSM-5 was synthesized from a gel with molar composition 0.13 TPABr : 1.12 NH₄F :
493 0.015Al₂O₃ : 1.0 SiO₂ : 57.87 H₂O. First, aluminum sulfate octadecahydrate (98 wt%,
494 Sigma-Aldrich) and tetrapropylammonium bromide (98 wt%, Sigma-Aldrich) were
495 dissolved in half of the above molar amount of deionized water to get a clear solution.
496 After that tetraethyl orthosilicate (98 wt%, Sigma-Aldrich) was added under stirring. The
497 resultant mixture was hydrolyzed overnight at room temperature to get a clear monophasic
498 solution. Then the NH₄F was dissolved in the second half of the molar amount of the
499 deionized distilled water, and the resultant solution was added slowly into the monophasic
500 solution under mechanical stirring. The resultant gel was vigorously stirred for 1 h, and
501 transferred to a 1000 mL Teflon-lined stainless steel autoclave. The synthesis was
502 conducted at 150 °C under static conditions. After 7 days of heating, the autoclave was
503 taken out from the oven and quenched immediately in cool tap water. The solids were
504 recovered by vacuum filtration and subsequently washed with deionized water. The solid
505 cake was then recovered and dried at 100 °C overnight. The template was removed by

506 calcination at 550 °C for 12 h with a ramp of 6 °C / min. The Si/Al ratio of the ZSM-5
507 samples is 91 and the samples was denoted ZSM-5(91).

508
509 Silicalite-1 was synthesized using the same initial reactants and preparation procedure.
510 The molar composition of the initial system was 0.13 TPABr : 0.94 NH₄F : 1.0 SiO₂ :
511 19.29 H₂O. The synthesis was performed at 170 °C for 10 days. A post-synthesis
512 treatment similar to the one applied to ZSM-5 was applied.

513
514 A low silica ZSM-5 sample synthesized in basic medium was included in the study to
515 evaluate the impact of synthesis medium and the high alumina content on the dissolution
516 process. The sample was provided by Clariant. The Si/Al ratio was 21 and the sample was
517 denoted ZSM-5(21).

518 *Fluoride medium etching*

519
520 Fluoride medium etching of MFI-type material was carried out in NH₄F (98.0%, Sigma-
521 Aldrich) aqueous solution using the following procedure: 7.5 g of the parent, calcined
522 ZSM-5 zeolite was dispersed in 200 g of 40 wt.% NH₄F aqueous solution and was allowed
523 to react at 50 °C for 20, 40 and 60 min under mechanical stirring and ultrasonic radiation
524 (USC 600 TH, 45 kHz, VWR). Intermediate samples were taken out after a set period of
525 reaction time. The etched products were thoroughly washed with deionized water after the
526 fluoride medium treatment.

527 *Characterization*

528
529 X-ray diffraction (XRD) measurements were performed on an X'pert Pro PANalytical
530 Diffractometer using Cu K α radiation ($\lambda = 1.5418 \text{ \AA}$, 45 kV, 40 mA). The samples were
531 studied in the 5-50° 2 θ range with a scanning step of 0.0167° s⁻¹.

532 Nitrogen adsorption-desorption experiments were performed with a Micromeritics ASAP
533 2020 automated gas adsorption analyzer. Prior to analysis, the samples were outgassed at
534 100 °C for 1 h and 300 °C for 12 h.

535
536 The Si and Al contents were determined by inductively coupled plasma optic emission
537 spectroscopy (ICP-OES) on an OES 5100 VDV ICP from Agilent; all samples are
538 digested in aqua regia and HF prior to the analysis.

539 *Ex situ scanning probe microscopy*

540
541 Atomic force microscopy (AFM) measurements of the MFI samples were performed on
542 an Asylum Research Cypher ES Environmental instrument (Santa Barbara, CA) equipped
543 with a liquid sample cell. The silicalite-1 crystals were dispersed on quickset Loctite
544 Epoxy (Henkel Corporation), which was affixed on a 15 mm specimen disc (Ted Pella,
545 Inc.). The epoxy was cured in an oven at 50 °C, and after 24 h, the sample disc was
546 removed, cooled to room temperature, and sonicated in deionized water (DI) to remove
547 loosely bound crystals. The sample disc was then placed in a closed liquid cell. A drop of
548 DI water was deposited on the sample substrate, which in contact with the AFM cantilever
549 (Oxford Instrument, non-coated silicon nitride), generates an aqueous interface for
550 scanning zeolite surfaces. Images of selected untreated crystals were first collected. The
551 sample disc was then treated in 40 wt% NH₄F solution (NH₄F salt, Sigma-Aldrich 98%) at
552 room temperature. At 5 min intervals, the sample disc was removed from the NH₄F
553 solution, washed with DI water, and scanned by AFM. Due to possible debris on crystal
554 surfaces after each treatment, the selected crystals were cleaned in contact mode before
555 the cantilever was exchanged with a new one for actual imaging. Between treatment

556 intervals, the sample disc was kept submerged in DI water. As initially tracked crystals
557 became unbound from the epoxy after a sequence of treatments, multiple crystals were
558 tracked during the first 60 min of treatment. Images ($2 \times 2 \mu\text{m}^2$ or $3 \times 3 \mu\text{m}^2$) were
559 collected by moving the cantilever in the x and y-direction on the crystal at set increment.
560 The obtained images were reassembled by overlapping segments to compose an image of
561 a significant portion of the crystal (Scheme S1, Supporting Information), which allows for
562 *ex situ* tracking of feature changes as treatment progressed.

563 *Time of flight secondary ion mass spectroscopy (ToF-SIMS)*

564 Sample preparation: The top mount holder is typically used to handle samples that are
565 very thick (few mm) or large (few cm). Samples are held in place using double-face
566 carbon. The sample holder was attached to the transfer arm by means of a bayonet fitting,
567 and then the latter is introduced in the load lock chamber until the vacuum pumping
568 reaches a vacuum of 5.0×10^{-5} mbar, ensuring an appropriate detection limit (few ppm).

569 Mass Spectroscopy: Positive and negative high mass resolution spectra were performed
570 using a TOF-SIMS NCS instrument, which combines a TOF-SIMS instrument (ION-TOF
571 GmbH, Münster, Germany) and an *in situ* scanning probe microscope (NanoScan,
572 Switzerland) at Shared Equipment Authority from Rice University. A bunched 30 keV
573 Bi^{3+} ions (with a measured current of 0.15 pA) was used as a primary probe for analysis
574 (scanned area $300 \times 300 \mu\text{m}^2$) with a raster of 128×128 pixels. A charge compensation
575 with an electron flood gun has been applied during the analysis. An adjustment of the
576 charge effects has been operated using a surface potential of -120 V and an extraction bias
577 of 0 V for the positive polarity and a surface potential of 90 V and an extraction bias of -
578 20 V for the negative polarity. The cycle time was fixed to 90 μs (corresponding to
579 $m/z = 0 - 737$ atomic mass unit (a.m.u) mass range).

580 2D imaging: A bunched 60 keV Bi^{3+} ions (with a measured current of 0.3 pA) was used as
581 primary probe for analysis (scanned area $50 \times 50 \mu\text{m}^2$) with a raster of 2048×2048 pixels
582 and then binned to enhance the signal-to-noise ratio. Same conditions of charge
583 compensation have been applied in imaging and in spectroscopy. The number of scans has
584 been limited to 5 for preventing the damage induced by a high dose of bismuth ions.

585 The same areas have been analyzed before and after the treatment. Each localized regions
586 of interest have been marked by reference points to provide the highest analysis accuracy
587 in the comparison.

588 *Electron microscopy*

589 Electron beam imaging and analysis were performed at the Central Facility for Advanced
590 Microscopy and Microanalysis at the University of California at Riverside.
591 Scanning/transmission electron microscopy (S/TEM) imaging was performed at 80 and
592 300 kV accelerating voltages in a ThermoFisher Scientific Titan Themis 300 instrument,
593 fitted with X-FEG electron source, 3 lens condenser system and S-Twin objective lens.
594 High-resolution TEM images were recorded at a resolution of 2048×2048 pixels with a
595 ThermoFisher CETA-16M CMOS digital camera with beam convergence semi-angle of
596 about 0.08 mrad. STEM imaging was performed at 300 kV accelerating voltage in the
597 Titan Themis 300 instrument. STEM images were recorded at probe convergence of 10
598 mrad with a probe current of 150 pA, using Fischione Instruments Inc. Model 3000 High
599 Angle Annular Dark Field (HAADF) detector at a frame size of 2048×2048 pixels, dwell
600 time of 15 $\mu\text{sec}/\text{pixel}$, and camera length of 245 mm.

601 TEM sample preparation: For the S/TEM analyses, a small amount of dry reaction powder
602 samples was dispersed in distilled water and ultrasonicated for 5 mins to break apart any
603
604
605

606 formed aggregates. A droplet of the resulting suspension was deposited on a TEM grid
607 covered with a thin holey carbon support film.

608
609 Thin foils for S/TEM imaging were prepared from individual MFI crystals by cutting thin
610 sections perpendicular the c-axis, following established ion milling procedures in a
611 scanning electron microscope/focused ion beam (SEM/FIB) instrument using Ga ion
612 source (Quanta 200i 3D, ThermoFisher Scientific). First, a strap of 5 μm thick protective
613 Carbon layer was deposited over a region of interest using the ion beam. Subsequently,
614 approximately 80 nm thin lamella was cut and polished at 30 kV and attached to a TEM
615 grid using in situ Oxford Instrument Autoprobe200 manipulator. To reduce surface
616 amorphization and Gallium implantation final milling at 5 kV and 0.5 nA was used to thin
617 the sample to electron transparency.

618
619 Scanning electron microscopy (SEM): a ThermoFisher Scientific Co. NovaNano SEM450
620 was used to study the morphology of the samples. SEM images were acquired using the
621 secondary and backscattered electron mode with a dedicated detector at 2, 5, and 15 kV
622 accelerating voltages.

623 624 625 **References**

- 626
627 1. Report on global zeolite market; [https://www.grandviewresearch.com/press-release/global-](https://www.grandviewresearch.com/press-release/global-zeolite-market)
628 [zeolite-market](https://www.grandviewresearch.com/press-release/global-zeolite-market) (accessed November, 2020)
- 629 2. G. Harvey, L. S. Dent Glaser, Structure and Properties of Aluminosilicate Solutions and
630 Gels, in M.L. Ocelli, H.E. Robson (Eds.), Zeolite Synthesis, Symposium Series 398,
631 American Chemical Society, 1989, Washington D.C., 49-65.
- 632 3. A. I. Lupulescu, J. D. Rimer, In Situ Imaging of Silicalite-1 Surface Growth Reveals the
633 Mechanism of Crystallization. *Science* **344**, 729-732 (2014).
- 634 4. M. Kumar, M. K. Choudhary, J. D. Rimer, Transient modes of zeolite surface growth from
635 3D gel-like islands to 2D single layers. *Nature Comm.* **9**, 2129 (2018).
- 636 5. F. Schüth, *Curr. Opin. Solid State Mater. Sci.* **5**, 389–395 (2001).
- 637 6. M. Smaïhi, O. Barida, V. Valtchev, Investigation of the Crystallization Stages of LTA-Type
638 Zeolite by Complementary Characterization Techniques. *Eur. J. Inorg. Chem.* 4370-4377
639 (2003).
- 640 7. E. A. Eilertsen, M. Haouas, A. B. Pinar, N. D. Hould, R. F. Lobo, K. P. Lillerud, F. Taulelle,
641 NMR and SAXS Analysis of Connectivity of Aluminum and Silicon Atoms in the Clear Sol
642 Precursor of SSZ-13 Zeolite. *Chem. Mater.* **24** 571-578 (2012).
- 643 8. G. Melinte, V. Georgieva, M.-A. Springuel-Huet, A. Nossov, O. Ersen, F. Guenneau, A.
644 Gedeon, A. Palčić, K. N. Bozhilov, C. Pham-Huu, S. Qiu, S. Mintova, V. Valtchev, 3D
645 Study of the Morphology and Dynamics of Zeolite Nucleation. *Chem. Eur. J.* **21**, 18316-
646 18327 (2015).
- 647 9. S. Mintova, N. H. Olson, V. Valtchev, T. Bein, Mechanism of zeolite A nanocrystal growth
648 from colloids at room temperature. *Science* **283**, 958–960 (1999).
- 649 10. R. Aiello, F. Crea, A. Nastro, B. Subotić, F. Testa, Influence of cations on the
650 physicochemical and structural properties of aluminosilicate gel precursors. Part 1. Chemical
651 and thermal properties. *Zeolites* **11**, 767-775 (1991).

- 652 11. V. Valtchev, S. Rigolet, K. N. Bozhilov, Gel evolution in a FAU-type zeolite yielding system
653 at 90 °C. *Micropor. Mesopor. Mater.* **101**, 73-82 (2007).
- 654 12. L. Ren, C. Li, F. Fan, Q. Guo, D. Liang, Z. Feng, C. Li, S. Li, F.- S. Xiao, UV-Raman and
655 NMR spectroscopic studies on the crystallization of zeolite A and a new synthetic route.
656 *Chem. Eur. J.* **17**, 6162-6169 (2011).
- 657 13. D. P. Petry, M. Haouas, S. C. C. Wong, A. Aerts, C. E. A. Kirschhock, J. A. Martens, S. J.
658 Gaskell, M. W. Anderson, F. Taulelle, Connectivity Analysis of the Clear Sol Precursor of
659 Silicalite: Are Nanoparticles Aggregated Oligomers or Silica Particles? *J. Phys. Chem. C*
660 **113**, 20827-20836 (2009).
- 661 14. B. Slater, T. Ohsuna, Z. Liu, O. Terasaki, Insights into the crystal growth mechanisms of
662 zeolites from combined experimental imaging and theoretical studies. *Faraday Discuss.* **136**,
663 125-141 (2007).
- 664 15. P. Cubillas, S. M. Stevens, N. Blake, A. Umemura, C. B. Chong, O. Terasaki, M. W.
665 Anderson, AFM and HRSEM Investigation of Zeolite A Crystal Growth. Part 1: In the
666 Absence of Organic Additives. *J. Phys. Chem. C* **115**, 12567-12574 (2011).
- 667 16. W. H. Dokter, H. F. van Garderen, T. P. M. Beleen, R. A. van Santen, V. Bras,
668 Homogeneous versus Heterogeneous Zeolite Nucleation. *Angew. Chem. Int. Ed. Engl.* **34**,
669 73-75 (1995).
- 670 17. F. K. Crundwell, The dissolution and leaching of minerals mechanisms, myths and
671 misunderstandings. *Hydrometallurgy* **139**, 132-148 (2013).
- 672 18. F. K. Crundwell, The mechanism of dissolution of minerals in acidic and alkaline solutions:
673 Part I - a new theory of non-oxidation dissolution. *Hydrometallurgy* **149**, 252-264 (2014).
- 674 19. F. K. Crundwell, The mechanism of dissolution of minerals in acidic and alkaline solutions:
675 Part II application of a new theory to silicates, aluminosilicates and quartz. *Hydrometallurgy*
676 **149**, 265-275 (2014).
- 677 20. F. K. Crundwell, On the mechanism of the dissolution of quartz and silica in aqueous
678 solutions. *ACS Omega* **2(3)**, 1116-1127 (2017).
- 679 21. M. Milina, S. Mitchell, P. Crivelli, D. Cooke, J. Pérez-Ramírez, Mesopore quality determines
680 the lifetime of hierarchically structured zeolite catalysts. *Nat. Commun.* **5**, 3922 (2014).
- 681 22. Z. Qin, J.-P. Gilson, V. Valtchev, Mesoporous zeolites by fluoride etching. *Curr. Opin.*
682 *Chem. Eng.* **8**, 1-6 (2015).
- 683 23. N. Linares, F. G. Cirujano, D. E. De Vos, J. García-Martínez, Surfactant-templated zeolites
684 for the production of active pharmaceutical intermediates. *Chem. Commun.* **55**, 12869-12872
685 (2019).
- 686 24. S. Van Donk, A. H. Janssen, J. H. Bitter, K. P. de Jong, Generation characterization, and
687 impact of mesopores in zeolite catalysts. *Cat. Rev. Sci. Eng.* **45**, 297-319 (2003).
- 688 25. S. M. T. Almutairi, B. Mezari, E. A. Pidko, P. C. M. M. Magusin, E. J. M. Hensen, Influence
689 of Steaming on the Acidity and the Methanol Conversion Reaction of HZSM-5 Zeolite. *J.*
690 *Catal.* **307**, 194-203 (2013).
- 691 26. L. R. Aramburo, L. Karwacki, P. Cubillas, S. Asahina, D. A. M. de Winter, M. R. Drury, I.
692 L. C. Buurmans, E. Stavitski, D. Mores, M. Daturi, P. Bazin, P. Dumas, F.
693 Thibault-Starzyk, J. A. Post, M. W. Anderson, O. Terasaki, B. M. Weckhuysen, Porosity,
694 Acidity, and Reactivity of Dealuminated Zeolite ZSM- 5 at the Single Particle Level: The
695 Influence of the Zeolite Architecture. *Chem. Eur. J.* **17**, 13773-13781 (2011).

- 696 27. R. M. Barrer, M. B. Makki, Molecular sieve sorbents from clinoptilolite. *Can. J. Chem.* **42**,
697 1481-1487 (1964).
- 698 28. M. Tromp, J. A. van Bokhoven, M. T. Garriga Oostenbrink, J. H. Bitter, K. P. de Jong, D. C.
699 Koningsberger, Influence of the Generation of Mesopores on the Hydroisomerization
700 Activity and Selectivity of n-Hexane over Pt/Mordenite. *J. Catal.* **190**, 209-214 (2000).
- 701 29. M. Ogura, S. Shinomiya, J. Tateno, Y. Nara, M. Nomura, E. Kikuchi, M. Matsukata, Alkali-
702 treatment technique — new method for modification of structural and acid-catalytic
703 properties of ZSM-5 zeolites. *Appl. Catal. A Gen.* **219**, 33-43 (2001).
- 704 30. M. K. Wardani, G. T. M. Kadja, A. T. N. Fajar, Subagjo, I. G. B. N. Makertihartha, M. L.
705 Gunawan, V. Suendo, R. R. Mukti, Highly crystalline mesoporous SSZ-13 zeolite obtained
706 via controlled post-synthetic treatment. *RSC Adv.* **9**, 77-86 (2019).
- 707 31. Z. Qin, G. Melinte, J.-P. Gilson, M. Jaber, K. Bozhilov, P. Boullay, S. Mintova, O. Ersen, V.
708 Valtchev, The Mosaic Structure of Zeolite Crystals. *Angew. Chem. Int. Ed.* **55**, 15049-15052
709 (2016).
- 710 32. Z. Qin, L. Pinard, M. A. Benghalem, T.J. Daou, G. Melinte, O. Ersen, S. Asahina, J.-P.
711 Gilson, V. Valtchev, Preparation of Single-Crystal “House-of-Cards”-like ZSM- 5 and Their
712 Performance in Ethanol-to-Hydrocarbon Conversion. *Chem. Mater.* **31**, 4639-4648 (2019).
- 713 33. L. Karwacki, M. H. F. Kox, D. A. M. deWinter, M. R. Drury, J. D. Meeldijk, E. Stavitski, W.
714 Schmidt, M. Mertens, P. Cubillas, N. John, A. Chan, N. Kahn, S. R. Bare, M. Anderson, J.
715 Kornatowski, B. M. Weckhuysen, Morphology-Dependent Zeolite Intergrowth Structures
716 Leading to Distinct Internal and Outer-Surface Molecular Diffusion Barriers. *Nature Mater.*
717 **8**, 959-965 (2009).
- 718 34. S. Kumar, T. M. Davis, H. Ramanan, R. Lee Penn, M. Tsapatsis, Aggregative Growth of
719 Silicalite-1. *J. Phys. Chem. B* **111(13)** 3398-3403 (2007).
- 720 35. J. D. H. Donnay, D. Harker, A new law of crystal morphology extending the Law of Bravais.
721 *Am. Mineral.* **22(5)**, 446-467 (1937).
- 722 36. P. Hartman, W. G. Perdok, On the relations between structure and morphology of crystals I.
723 *Acta Cryst.* **8(1)**, 49-52 (1955).
- 724 37. T. M. Davis, T. O. Drews, H Ramanan, C. He, J. Dong, H. Schnablegger, M. A. Katsoulakis,
725 E. Kokkoli, A. V. McCormick, R. Lee Penn, M. Tsapatsis, Mechanistic Principles of
726 Nanoparticle Evolution to Zeolite Crystals. *Nature Mater.* **5(5)**, 400-408 (2006).
- 727 38. J. J. De Yoreo, P. U. P. A. Gilbert, N. A. J. M. Sommerdijk, R. L. Penn, S. Whitlam, D.
728 Joester, H. Z. Zhang, J. D. Rimer, A. Navrotsky, J. F. Banfield, A. F. Wallace, F. M. Michel,
729 F. C. Meldrum, H. Colfen, P. M. Dove, Crystallization by Particle Attachment in Synthetic,
730 Biogenic, and Geologic Environments. *Science* **349**, aaa6760 (2015).
- 731 39. J. R. Agger, N. Hanif, C. S. Cundy, A. P. Wade, S. Dennison, R. A. Rawlinson, M. W.
732 Anderson, Silicalite Crystal Growth Investigated by Atomic Force Microscopy. *J. Am. Chem.*
733 *Soc.* **125**, 830-839 (2003).
- 734 40. C. G Darwin, The reflexion of X-rays from imperfect crystals. *Philosoph. Magazine* **43**, 800-
735 829 (1922).
- 736
737
738
739
740

Acknowledgments

V. V. acknowledges the financial support from the Industrial Chair ANR-TOTAL “NanoClean Energy” (ANR-17-CHIN-0005-01) and FEDER 18P01675. KNB acknowledges the support for the analytical work by the Office of the Vice-Chancellor of Research and Economic Development at the University of California at Riverside. JDR received support primarily from the U.S. Department of Energy, Office of Science, Office of Basic Energy Sciences under Award Number DE-SC0014468, and additional support provided by the Welch Foundation (Award E-1794). ToF-SIMS analysis was carried out with support provided by the National Science Foundation under Award CBET-1626418. This work was conducted in part using resources of the Shared Equipment Authority at Rice University.

Author contributions: Z.Q. and A.P. prepared the zeolite crystals and performed the dissolution experiments and the general characterization of the samples. K.N.B. performed the electron microscopy study; T.T.L. performed the AFM study; T.T. performed the ToF-SIMS study. V.V. led the overall design and direction of the project. K.N.B., J.D.R. and V.V. prepared the manuscript with help from all authors.

Competing interests: The authors declare no competing interests.

Data and materials availability: All data needed to evaluate the conclusions in the paper are present in the paper and/or the Supplementary Materials.